Sidewall oxide effects on spin-torque- and magnetic-field-induced reversal characteristics of thin-film nanomagnets

O. OZATAY[1,2]*, P. G. GOWTHAM[1], K. W. TAN[1], J. C. READ[1], K. A. MKHOYAN[1], M. G. THOMAS[1], G. D. FUCHS[1], P. M. BRAGANCA[1], E. M. RYAN[1], K. V. THADANI[1], J. SILCOX[1], D. C. RALPH[1] AND R. A. BUHRMAN[1]

[1]Cornell University, Ithaca, New York 14853-2501, USA
[2]Hitachi Global Storage Technologies, San Jose Research Center, San Jose, California 95136, USA
*e-mail: ozhan.ozatay@hitachigst.com

Published online: 8 June 2008; doi:10.1038/nmat2204

The successful operation of spin-based data storage devices depends on thermally stable magnetic bits. At the same time, the data-processing speeds required by today's technology necessitate ultrafast switching in storage devices. Achieving both thermal stability and fast switching requires controlling the effective damping in magnetic nanoparticles. By carrying out a surface chemical analysis, we show that through exposure to ambient oxygen during processing, a nanomagnet can develop an antiferromagnetic sidewall oxide layer that has detrimental effects, which include a reduction in the thermal stability at room temperature and anomalously high magnetic damping at low temperatures. The *in situ* deposition of a thin Al metal layer, oxidized to completion in air, greatly reduces or eliminates these problems. This implies that the effective damping and the thermal stability of a nanomagnet can be tuned, leading to a variety of potential applications in spintronic devices such as spin-torque oscillators and patterned media.

How the native oxides that form at the surface of a ferromagnet affect magnetic properties has long been a subject of intensive research[1–3]. These surface oxides are usually antiferromagnetic and can alter the magnetic behaviour of the ferromagnet by introducing extra anisotropies via exchange bias effects below a critical temperature T_B (refs 4–6). The interfacial coupling can lead to shifts in hysteresis loops and increases in coercivity, both of which are manifestations of a change in the energy landscape that makes one magnetic orientation of the ferromagnetic element favourable over another. The strength of this exchange bias is a strong function of the microstructural properties of both the ferromagnetic material and its oxide, such as grain size distribution, structural defects, interfacial roughness and variations in chemical composition, because of the role of these properties in determining the density of uncompensated spins near the antiferromagnet–ferromagnet interface[7]. Here, we show that the presence of such an adventitious oxide layer just on the sidewalls of a patterned thin-film nanomagnet, the top and bottom of which are passivated via contact to normal-metal spacer layers, can have a major impact on the magneto-electronic behaviour of the nanomagnet by substantially reducing its room-temperature thermal stability and by providing a path for increased energy dissipation, leading to higher damping at low temperatures[8].

Before studying nanofabricated devices, we analysed the surface chemistry of air-exposed Py films and also Py films coated with a 1.5 nm overlayer of Al before air exposure to suppress magnetic oxide formation, using X-ray photoemission spectroscopy and electron energy loss spectroscopy techniques (see Supplementary Information, Methods). For the surface of air-exposed Py, these measurements indicate the existence of antiferromagnetic NiO, FeO and Fe_2O_3, with a total oxide thickness of 20 ± 4 Å, in good agreement with previous measurements based on polarized-neutron reflectometry[9]. For the Al-coated Py films, the oxidation of the Ni component of the Py layer is fully suppressed. We do find some presence of oxidized Fe (Fe^{+3}) following the exposure of Al-coated Py to air, but in a form where the Fe ions are dispersed within the AlO_x layer, so that their magnetic interactions should be weak. We conclude that an AlO_x passivation layer can be successful in greatly reducing or eliminating the formation of antiferromagnetic surface oxides on Py.

To examine the role of surface oxides at the sidewalls of a thin-film nanomagnet on its magnetic and magneto-transport properties, we sputter deposited Py(2)/Cu(120)/Py(20)/Cu(12)/Py(4)/Cu(12)/Pt(4) nm multilayers onto a 500 nm layer of SiO_2 on a Si substrate, and patterned them into spin-valve nanopillars using three different treatments for the sidewalls of the device. The cross-section of the device geometry is shown schematically in Fig. 1a. The first set of devices was protected from sidewall oxidation with the *in situ* deposition of 1.5-nm-thick Al, which was subsequently oxidized in air (device type A). A high-magnification cross-sectional bright-field scanning transmission electron microscopy image of a type-A device is shown in Fig. 1b. The AlO_x coating of the sidewalls is clearly visible and suggests a successful, conformal Al deposition. The second set of devices (type B) served as control samples and their sidewalls were exposed to air before they were

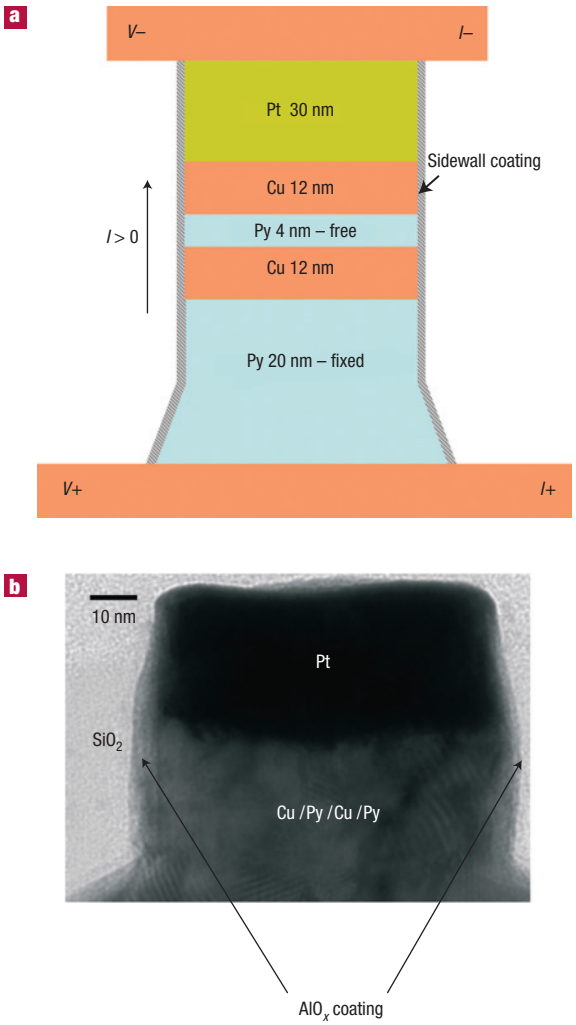

Figure 1 Cross-sectional view of a nanopillar spin-valve device. a, Schematic diagram of a Py (20 nm) fixed layer /Cu (12 nm) spacer/Py (4 nm) free-layer nanopillar spin-valve device, the sidewalls of which can be subjected to different oxidation conditions. **b**, A high-resolution bright-field transmission electron microscope cross-sectional image of an AlO_x-passivated device. A careful examination of the sidewalls provides evidence for the successful conformal coating with an AlO_x passivation layer (courtesy of Intel).

covered by a SiO_2 insulation layer to achieve electrical isolation of individual devices. The last set of devices (type C) had a 2.5 nm NiO coating deposited on top of the air-oxidized sidewalls to facilitate the study of strong exchange coupling at the sidewall. All of the nanopillar devices were patterned to have $70 \times 30\ nm^2$ elliptical cross-sections. In these devices, the thin Py layer acts as the magnetic 'free layer' because it has a substantially lower coercive field in comparison with the thicker Py 'fixed' layer.

Figure 2a shows the spin-torque switching behaviour of a type-A nanopillar device at 4.2 K with an applied field that cancels the average dipole field from the fixed layer. In all of our spin-torque plots, positive current flows from the fixed to the free layer (electrons from free to fixed). We designate the parallel-to-antiparallel (P-to-AP) switching current and the antiparallel-to-parallel (AP-to-P) switching currents as I_c^+ and I_c^-, respectively. As the switching events at low temperatures are not significantly thermally assisted, peaks and shoulders in the differential resistance are observed in Fig. 2a before the switching points, corresponding to the onset of small-angle precessional dynamics before switching[10,11]. We define the thresholds for the pre-switching dynamics as I_d^+ and I_d^- for P-to-AP and AP-to-P switching, respectively. Figure 2b shows a typical minor loop of the free-layer magnetoresistance response at 4.2 K for a type-A sample. The magnetic hysteresis parameters of interest are the half-width of the minor loop, which we refer to as the coercive field H_c, and the shift of the centroid of the loop from the origin, which we refer to as the effective dipole field H_d.

To compare the effects of the Al passivation layer and the native oxide on the room-temperature magnetic behaviour of the free-layer nanomagnets, we measured H_c, as determined by minor loop magnetoresistance scans similar to that in Fig. 2b, for 30 different samples each of type-A and type-B nanopillars. The results were $\langle H_c \rangle_A = 87 \pm 43$ Oe and $\langle H_c \rangle_B = 38 \pm 38$ Oe (where the uncertainties are the standard deviations), with almost half of the control samples (type B) being superparamagnetic ($H_c = 0$). The average room-temperature magnetoresistance of the devices was $\langle \Delta R \rangle_A = 105 \pm 12\ m\Omega$ and $\langle \Delta R \rangle_B = 101 \pm 12\ m\Omega$, which demonstrates a small sample-to-sample variation in the cross-sectional area of the nanopillars despite the wide variation in H_c. The large difference between the average values of H_c for the type-A and type-B samples shows that a thin antiferromagnetic oxide just on the sidewalls of a patterned thin-film nanomagnet can have a major impact on its magnetic stability, even above the antiferromagnetic blocking temperature of the oxide. (The blocking temperatures of the surface oxides are well below room temperature as discussed below.)

To further quantify this result, we measured the effective activation energies E_a for both spin-torque-driven and magnetic-field-driven magnetic reversal for spin-valve devices of both type A and B. To determine E_a for a given sample, we measured the average spin-torque reversal current $\langle I_c \rangle$ and the magnetic reversal field $\langle H_{rev} \rangle$ as a function of the ramp rates of current and magnetic field, respectively, over two or more decades of variation in ramp rate. The results of typical ramp rate measurements are shown for a type-A device in Fig. 2c,d. The data were then analysed by fitting to the Kurkijarvi[12,13] model and to the Sharrock[14] model respectively. In these models, we have

$$\langle I_c \rangle = I_{c0}\left[1 - \frac{k_B T}{E_a}\ln\left(\frac{k_B T |I_{c0}|}{\tau_0 E_a |R_I|}\right)\right],$$

$$\langle H_c \rangle = H_{c0}(T)\left\{1 - \left[\frac{k_B T}{E_a}\ln\left(\frac{1}{\tau_0 |R_H| \ln 2}\right)\right]^{2/3}\right\}, \qquad (1)$$

where I_{c0} is the spin-torque reversal current in the absence of thermal fluctuations, k_B is Boltzmann's constant, H_{c0} is the coercive (anisotropy) field in the absence of thermal fluctuations, R_I and R_H are the ramp rates for current and field, $H_c = H_{rev} - H_d$ and τ_0 is the characteristic fluctuation attempt time, which we assume to be 1 ns. From the slopes of the fits shown in Fig. 2c,d, we obtain for P-to-AP switching $E_{a+} = 1.78 \pm 0.17$ eV and $I_{c0}^+ = 1.93 \pm 0.09$ mA from the current sweeps and $E_{a+} = 2.02 \pm 0.14$ eV and $H_{c0}^+ = 245 \pm 8$ Oe from the field sweeps, and for AP-to-P switching $E_{a-} = 1.52 \pm 0.06$ eV and $I_{c0}^- = -1.86 \pm 0.05$ mA from the current sweeps and $E_{a-} = 1.43 \pm 0.09$ eV and $H_{c0}^- = 296 \pm 12$ Oe from the field sweeps. (The difference between E_{a+} and E_{a-} in these measurements is consistent with micromagnetic simulations that show that the dipole field from the fixed layer gives a stronger perturbation on the free layer when it is in the antiparallel rather than the parallel orientation.) Repeating these measurements for 10 type-A and

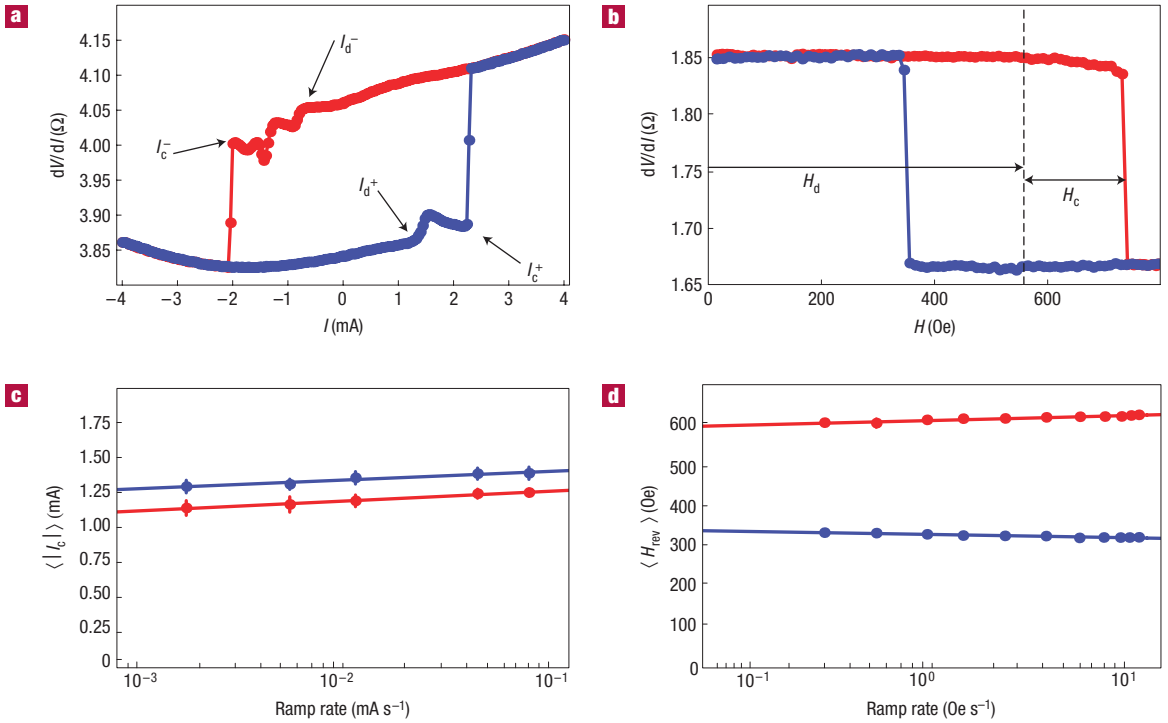

Figure 2 Spin-torque switching and magnetic-field-induced switching characteristics of an Al-passivated device. a, Current scan taken at 4.2 K demonstrating a characteristic spin-torque switching curve. The switching currents are labelled I_c^+ and I_c^- for P-to-AP (blue) and AP-to-P (red) switching, respectively. The currents for the onset of precessional dynamics are labelled I_d^+ and I_d^-. **b**, Magnetic-field scan at 4.2 K showing the minor loop of the free layer. The loop shift from zero applied field is labelled as H_d (the effective dipolar field) and the half-width of the hysteresis loop is labelled as H_c (the coercive field). **c**, Average critical currents measured at room temperature, as a function of the logarithm of the current ramp rate, for 20 measurements at each ramp rate value. **d**, Average coercive fields measured at room temperature, as a function of the logarithm of the field ramp rate, for 20 measurements at each ramp rate value. The solid lines in **c** and **d** (blue for P-to-AP and red for AP-to-P switching) are fits used to determine the energy barriers for switching.

type-B samples, we find a marked difference in the average effective activation barriers for the two sample types: $\langle E_a \rangle = 1.8 \pm 0.2$ eV, $\langle H_{c0} \rangle = 290 \pm 20$ Oe and $\langle |I_{c0}| \rangle = 1.75 \pm 0.25$ mA for type-A devices, and $\langle E_a \rangle = 0.9 \pm 0.2$ eV, $\langle H_{c0} \rangle = 156 \pm 20$ Oe and $\langle |I_{c0}| \rangle = 1.65 \pm 0.25$ mA for type-B devices, not including superparamagnetic ones.

We attribute the large difference between the activation barrier of the AlO_x-passivated nanomagnets and that of the control nanomagnets to a substantial reduction in the amount of antiferromagnetic oxide on the sidewalls of the AlO_x-passivated samples. This reduces magnetic disorder caused by local fluctuations in the exchange coupling at the boundaries of the nanomagnet and its native oxide. The energy barrier for magnetic reversal is affected by this disorder[15] even above the blocking temperature of the antiferromagnetic oxide, because it is a source of dynamic non-uniformity that can open pathways for spatially non-uniform magnetization reversal. Previous experiments on single-crystal antiferromagnetic films coupled to ferromagnets have reported coercivity enhancements above the blocking temperature[16,17], in contrast to the reductions in energy barrier that we find. We believe the difference is that the native oxides in our samples do not have a well-defined crystalline orientation, but instead consist of a distribution of grains that induce fluctuating anisotropies in random directions yielding no net coercivity enhancement, but that enable inhomogeneous reversal mechanisms, thereby reducing the thermal stability of the free layer at room temperature.

For an idealized model in which the free-layer magnetization behaves as a single domain, the Néel–Brown prediction for the activation barrier is:

$$E_a = \frac{1}{2} H_{c0} M_s Vol, \qquad (2)$$

where M_s is the saturation magnetization (645 emu cm^{-3}) (ref. 18) and Vol is the magnetic volume. Using $\langle H_{c0} \rangle = 290$ Oe as determined by the fits, for our samples equation (2) predicts an energy barrier of 1.7 eV, in good agreement with the experimentally measured average energy barrier of 1.8 ± 0.2 eV for type-A samples. Typically, a deviation between measured activation barriers and the Néel–Brown prediction, such as we find for our type-B samples with a native oxide, is modelled by ascribing it to an 'effective volume' of the nanomagnet that is considerably less than its physical volume. In our samples, the presence of a ~2-nm-thick native oxide would produce less than a 5% change in the true physical volume of the nanomagnet, so that the reduced volume cannot account for the observed 50% reduction in the energy barriers. Instead, our results indicate that much of the reduction, at least at room temperature, can arise from coupling to the fluctuating spins of the antiferromagnetic surface oxides, and that a considerably more ideal energy barrier for a patterned thin-film nanomagnet can be obtained using AlO_x passivation.

To examine the temperature (T) dependence of the effects of the surface oxides, we measured $\langle I_c(T) \rangle$ and $\langle H_c(T) \rangle$, using constant ramp rates, from 300 to 4.2 K for the three different type

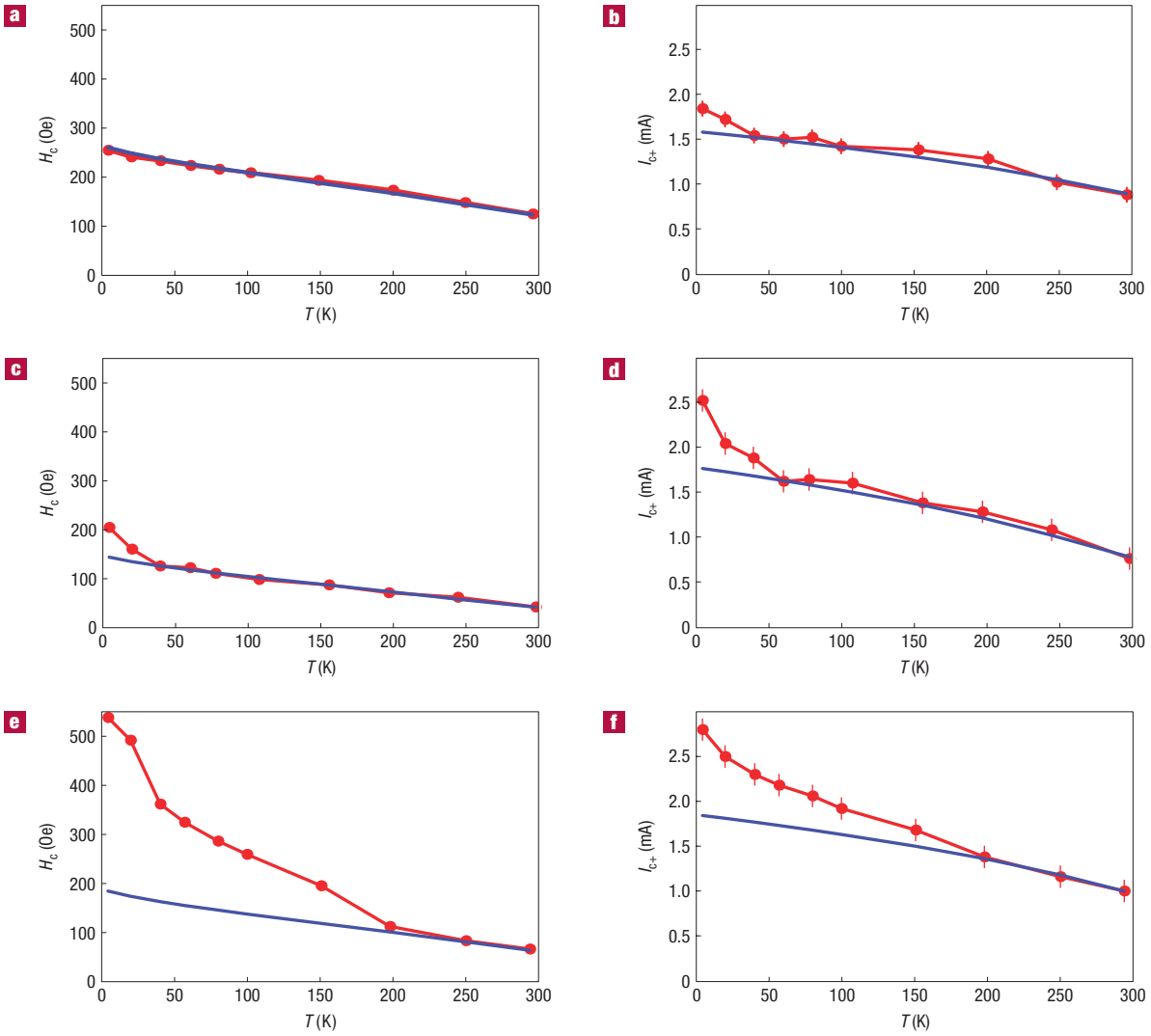

Figure 3 Temperature dependence of coercivity and spin-torque switching currents. The temperature dependence of $\langle H_c \rangle$ and $\langle I_c^+ \rangle$ (red circles) taken at constant ramp rates, along with fits (blue curves) to equation (1) for an AlO_x-passivated sample (**a**,**b**), a control sample with native oxide on its sidewalls (**c**,**d**) and a sample coated with 2.5 nm of NiO (**e**,**f**).

of sample. We compared the results with the values of $\langle I_c(T) \rangle$ and $\langle H_c(T) \rangle$ predicted by the Sharrock and Kurkijarvi models (equation (1)), assuming that I_{c0}, H_{c0} and E_a have temperature dependencies related to the saturation magnetization $M_S(T)$ as measured on an unpatterned Cu/Py(4 nm)/Cu multilayer film (we assume $I_{c0}(T) \propto M_S^2(T)$, $H_{c0}(T) \propto M_s(T)$ and $E_a(T) \propto M_S^2(T)$). As shown in Fig. 3a, $\langle H_c(T) \rangle$ for the type-A, AlO_x-passivated, samples is in very good accord with the Sharrock model over the entire temperature range. The coercive field measured at 4.2 K is also in good accord with the predictions of a micromagnetic simulation[19] of a nanomagnet with the experimental size and shape. Thus, these results confirm that the energy barrier we measure at room temperature for type-A nanomagnets is close to the ideal Néel–Brown prediction. $\langle H_c(T) \rangle$ for the type-B nanomagnets, with the native antiferromagnetic oxide on the sidewalls, exhibit both a low value of $\langle H_c \rangle$ at room temperature and a distinct upturn in the rate of increase of $\langle H_c(T) \rangle$ with decreasing T at ~40 K (Fig. 3c). Type-C samples, with 2.5 nm of NiO deposited on top of native oxide around the nanomagnet perimeter, exhibit sharp upturns in $\langle H_c(T) \rangle$ at both ~200 K and ~40 K, and quite high values of $\langle H_c(4.2\,\mathrm{K}) \rangle$ (Fig. 3e). The pronounced changes in the behaviour of $\langle H_c(T) \rangle$ at specific temperatures are indicative of an extra nanomagnet anisotropy becoming effective below the blocking temperature of an antiferromagnetic oxide, with the two-stage effect for type-C samples indicating separate blocking of two different oxides, $T_B = 40$ K for the native oxide and $T_B = 200$ K for the 2.5 nm NiO coating. Even though the native oxide has a substantial NiO component, this variation in blocking temperature can be explained as being due to differences in the average grain size and thickness[20,21], in addition to differences in composition. (Blocking temperatures in thin films are often very different from the bulk value for an antiferromagnetic oxide[22].)

Turning to the T dependence of the spin-torque reversal currents, shown in Fig. 3b,d,f, there is a strong correlation between the deviations of $\langle H_c(T) \rangle$ from the prediction of the thermally activated magnetic reversal model, and those of $\langle I_c(T) \rangle$ from the spin-torque reversal model. Whenever a sample is cooled through a

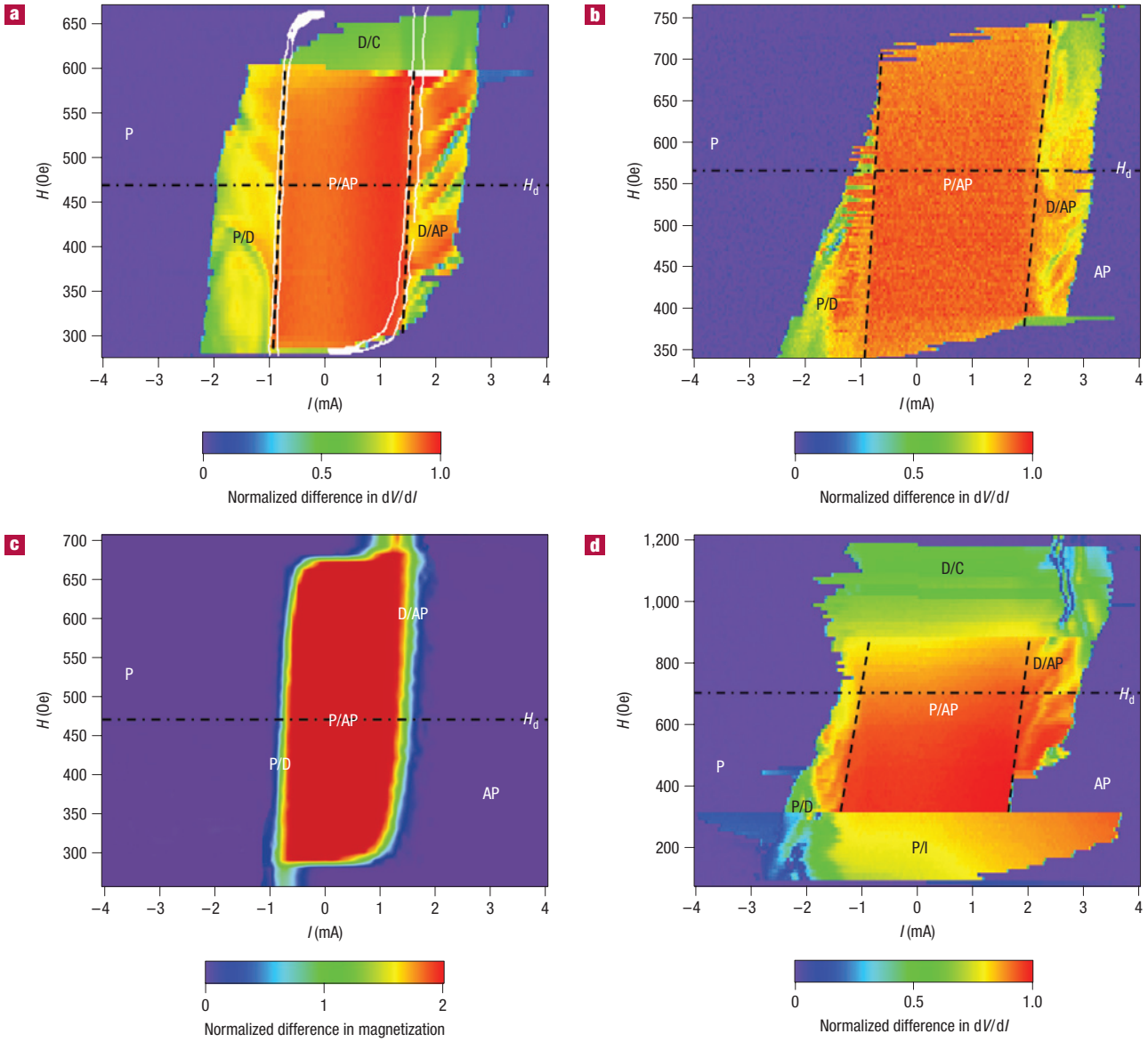

Figure 4 Spin-torque phase diagrams measured at 4.2 K. a–d, An AlO_x-passivated sample (**a**), a control sample (**b**) and a sample coated with 2.5 nm of NiO (**d**) compared with a macrospin simulation (**c**). The possible phases consist of the parallel state (P), the antiparallel state (AP), the intermediate state (I), the dynamic state (D) and curling (C). The horizontal dotted–dashed lines show approximately the applied field that cancels out the average dipole field on the free layer. The angled dashed lines represent the static/dynamic phase boundaries for the onset of dynamics to which the macrospin simulations are fitted. The white curves in **a** are the static/dynamic and magnetic-reversal phase boundaries computed by macrospin simulations.

temperature region where $\langle H_c(T)\rangle$ begins to increase more rapidly owing to the onset of antiferromagnetic blocking, there is a parallel increase in $\langle I_c(T)\rangle$. Within the macrospin approximation[23], the minimum current for the onset of spin-torque excited magnetic dynamics in a nanomagnet at $T = 0$ is given in centimetre-gram-second units by

$$I_{d,+/-} \approx 2\pi \frac{2e}{\hbar} \frac{\alpha}{\eta_{+/-}} M_s^2 Vol \qquad (3)$$

for the case where the thin-film demagnetization field, $\approx 4\pi M_s$, is much greater than the inplane anisotropy field. Here, α is the Gilbert damping parameter and η is the spin-torque efficiency. Thus, from equation (3), the increase in $\langle I_c\rangle$, which we can expect to scale with I_d, are not directly attributable to the changes in $\langle H_c\rangle$ or E_a, but instead can be ascribed to increases in the effective magnetic damping that begin whenever the antiferromagnetic oxide begins to block magnetically, thereby providing an extra magnetic relaxation pathway. Increases in magnetic damping below the blocking temperature are also observed in ferromagnetic/antiferromagnetic bilayers[24,25]. Note that even the AlO_x-passivated sample shows a modest low-T upturn in I_c, which indicates that spin-torque reversal currents may be a more sensitive low-T indicator of the presence of some residual antiferromagnetic oxide (perhaps the Fe_2O_3 component in the AlO_x layer discussed above) than the coercive fields.

To further quantify the effect of sidewall antiferromagnetic oxides on the low-T behaviour, we measured free-layer spin-torque reversal phase diagrams at 4.2 K for devices of each sample type (Fig. 4). These phase diagrams were constructed by taking differential resistance measurements as the function of bias current (dV/dI versus I) for applied magnetic fields that ranged over the hysteretic regime of the free layer, and plotting the difference between curves for the initially parallel and initially antiparallel configurations. The dashed lines in Fig. 4 indicate the phase boundaries for the onset of spin-torque excited dynamics as a function of H. We used these phase boundary measurements and the macrospin approximation[23] $dI_d/dH = (\alpha/\eta)(2e/\hbar)M_s Vol$ to obtain comparative values for the magnetic damping at 4.2 K of the three different types of sample, with the results being $\langle\alpha_B\rangle = 1.5\langle\alpha_A\rangle$ and $\langle\alpha_C\rangle = 1.6\langle\alpha_A\rangle$ under the assumption that the spin-torque efficiency η is approximately the same for all samples. Previous experiments have shown that low-temperature enhancements in the damping of oxidized permalloy films are greatly reduced by oxidation passivation, similar to our findings[3]. These different damping values provide a consistent explanation for the higher spin-torque reversal currents at 4.2 K for spin valves with antiferromagnetic oxides on the sidewalls, with the increased damping being attributed to the slow dragging of antiferromagnetic nano-oxide domains during dynamic precession.

It is important to note, however, that the macrospin approximation does not provide a complete description of the low-temperature behaviour of the spin-valve devices. This is illustrated in Fig. 4a, which shows the spin-torque phase diagram boundaries as calculated with the macrospin approximation using device parameter values, M_s and Vol, appropriate to our structures (white lines) together with the measured phase diagram of a type-A sample. In this calculation, we used the spin-torque efficiency function $\eta(\theta) = P/[(1+(1/\Lambda^2)) + (1-(1/\Lambda^2))\cos(\theta)]$ (from ref. 26), where P is the spin polarization of the current and the parameter Λ^2 determines the asymmetry of spin-torque efficiency as a function of the angle θ. We fit to the static/dynamic phase boundary lines in Fig. 4a using the two adjustable parameters P/α and Λ^2. In general, good fits can be obtained to the 4.2 K static/dynamic boundaries, but the experiments exhibit a much broader region between the onset of dynamics and the reversal current than is predicted by the macrospin simulation. This latter result could be due to several effects, including the coupling of spin-wave modes between the fixed and the free layers, non-uniform free-layer excitations due to the non-uniform dipole field and demagnetization effects, and in the case of type-B and type-C samples, local variations in the exchange coupling from the sidewall oxides. In addition, we sometimes observe a non-abrupt AP-to-P transition at the high-field edge of the hysteresis region of the phase diagram (indicated as a dynamics/curling (D/C) regime), and all type-C samples measured showed a very gradual decrease in dV/dI as the AP-to-P switching field was approached, with no apparent intermediate dynamic state (I). We attribute this non-ideal behaviour at the magnetic extremes of the hysteretic region to inevitable lithographic edge roughness and surface defects that can act as domain wall pinning centres and cause non-abrupt transitions, and, in the case of type-C samples, to a slow magnetization rotation due to a strong coupling to the perimeter oxides.

Returning our attention to the static/dynamic phase boundaries, which are fitted well by the macrospin model, if we assume a Py spin polarization of 0.48 (ref. 27), then the fit to the slope of the phase boundaries gives $\langle\alpha_A\rangle \approx 0.016$ at 4.2 K for the type-A samples. This is fairly comparable to, although ~60% larger than, the result obtained from recent room-temperature spin-torque ferromagnetic resonance measurements[28] on similar Py spin-valve devices, which yielded $\alpha_{Py} = 0.010 \pm 0.002$. These damping values, which are obtained from measurements of small-angle oscillations, are considerably smaller than the ones inferred by fitting the macrospin model to the time-domain current-pulse-driven reversal of Py spin-valve devices[8,18], which gave $\alpha_{Py} \sim 0.03$ at room temperature and ~0.06 at 4.2 K for Py spin valves with unpassivated sidewalls. These latter results are probably a consequence of the macrospin approximation not providing a good description of the large-amplitude magnetic dynamics during spin-torque-driven magnetic reversal.

In summary, we have found that a native antiferromagnetic oxide layer coating the sidewalls of a patterned Py thin-film nanomagnet can substantially affect both field-driven and spin-torque-driven switching of the nanomagnet, at both low and room temperature. Local fluctuations in exchange coupling and the slow dragging of antiferromagnetic nano-oxide domains during ferromagnetic precession provide mechanisms for energy dissipation, leading to increased extrinsic damping at low temperatures. The unstable oxide domains that are coupled to the Py nanomagnet at room temperature, above the antiferromagnetic blocking temperature of the oxide, can induce spatially non-uniform modes of magnetic reversal, which lead to a substantial reduction in the effective energy barrier for switching. We believe that antiferromagnetic native oxides at the edges of spin-transfer devices have affected the device performance significantly in perhaps all previous experiments in this field. We find that a passivation treatment, in which a thin Al layer is deposited on the sidewalls and allowed to oxidize, greatly reduces or eliminates these adverse antiferromagnetic oxide effects. The Al sidewall passivation treatment could be very important for producing the smallest possible thermally stable free-layer nanomagnet structures so as to reduce the required current for spin-torque reversal in magnetic memory applications, for enhancing the thermal stability of patterned media and also for obtaining high-quality-factor spin-torque oscillators via reduction in linewidths.

METHODS

The AlO_x passivation layer on the Py/Cu/Py nanopillar spin-valve devices was made by ion-beam depositing Al at three different angles of 20°, 45° and 75° with respect to the normal of a rotating sample stage, in a chamber with a base pressure of 1×10^{-7} torr, immediately after the end of the ion-mill nanopillar patterning step. In an effort to achieve a uniform coating of the sidewalls, a high Ar partial pressure (5.2 mtorr) was used. The Al coating was oxidized by exposure to ambient oxygen.

The free-layer minor loops were obtained by first applying a large easy-axis positive magnetic field to saturate the fixed layer and then sweeping the field back to zero. This conditions the spin valve to begin in the antiparallel state that is favoured by the device owing to the magnetic dipole field from the fixed layer. A subsequent field scan in the positive direction then measured the resistance changes due to the free-layer switching events.

The 4.2 K phase diagrams were constructed in the following way: for each scan, the data from one direction (P-to-AP switching) was subtracted from the other (AP-to-P switching), with the result normalized by ΔR to obtain plots for comparison between the different sample types. The corresponding macrospin simulation of the phase diagram for the evolution of easy-axis magnetization was obtained by a similar subtraction procedure. In the simulation, the magnetization was initialized to antiparallel or parallel states for AP-to-P or P-to-AP scans respectively. Then, the Landau–Lifshitz–Gilbert equation was evolved with a fixed current and field until a steady-state magnetization response was achieved. In this manner, the whole phase diagram was constructed. The simulation time was 5 ns with a simulation step time of 1 ps. A fourth-order Runge–Kutta solver was used to evolve the Landau–Lifshitz–Gilbert equation. Thermal fluctuations were accounted for by a Langevin field and a thermal (Boltzmann) distribution of initial states for the free layer. Each magnetization response was averaged over 100 trials. We used the spin-torque efficiency function $\eta(\theta) = P/[(1+(1/\Lambda^2)) + (1-(1/\Lambda^2))\cos(\theta)]$ (from ref. 26), with

fitting parameters P/α and Λ^2, where P is the spin polarization and α is the magnetic damping. For AlO_x-passivated samples, native oxide samples and NiO-coated native oxide samples, respectively, the best fit parameters were $P/\alpha = 30 \pm 1$, 20 ± 1, 18 ± 1 and $\Lambda^2 = 1.98 \pm 0.01$, 2.87 ± 0.01, 1.92 ± 0.01.

Received 3 January 2008; accepted 6 May 2008; published 8 June 2008.

References

1. Meiklejohn, W. H. & Bean, C. P. New magnetic anisotropy. *Phys. Rev.* **102**, 1413–1414 (1956).
2. Hagedorn, F. B. Exchange anisotropy in oxidized permalloy thin films at low temperatures. *J. Appl. Phys.* **38**, 3641–3645 (1967).
3. Patton, C. E. & Wilts, C. H. Temperature dependence of ferromagnetic resonance linewidth in thin Ni–Fe films. *J. Appl. Phys.* **38**, 3537–3540 (1967).
4. Nogues, J. *et al.* Exchange bias in nanostructures. *Phys. Rep.* **422**, 65–117 (2005).
5. Krivorotov, I. N., Leighton, C., Nogues, J., Schuller, I. K. & Dahlberg, E. D. Relation between exchange anisotropy and magnetization reversal asymmetry in Fe/MnF_2 bilayers. *Phys. Rev. B* **65**, 100402 (2002).
6. McMichael, R. D., Stiles, M. D., Chen, P. J. & Egelhoff, W. F. Ferromagnetic resonance studies of NiO-coupled thin films of $Ni_{80}Fe_{20}$. *Phys. Rev. B* **58**, 8605–8612 (1998).
7. Krishnan, K. M. *et al.* Exchange biasing of permalloy films by Mn_xPt_{1-x}: Role of composition and microstructure. *J. Appl. Phys.* **83**, 6810–6812 (1998).
8. Emley, N. C. *et al.* Time-resolved spin-torque switching and enhanced damping in permalloy/Cu/permalloy spin-valve nanopillars. *Phys. Rev. Lett.* **96**, 247204 (2006).
9. Fitzsimmons, M. R., Silva, T. J. & Crawford, T. M. Surface oxidation of permalloy thin films. *Phys. Rev. B* **73**, 014420 (2006).
10. Krivorotov, I. N. *et al.* Temperature dependence of spin-transfer-induced switching of nanomagnets. *Phys. Rev. Lett.* **93**, 166603 (2004).
11. Florez, S. H., Katine, J. A., Carey, M., Folks, L. & Terris, B. D. Modification of critical spin torque current induced by rf excitation. *J. Appl. Phys.* **103**, 07A708 (2008).
12. Kurkijarvi, J. Intrinsic fluctuations in a superconducting ring closed with a Josephson junction. *Phys. Rev. B* **6**, 832–835 (1972).
13. Myers, E. B. *et al.* Thermally activated magnetic reversal induced by a spin-polarized current. *Phys. Rev. Lett.* **89**, 196801 (2002).
14. Sharrock, M. P. Time-dependent magnetic phenomena and particle-size effects in recording media. *IEEE Trans. Magn.* **26**, 193–197 (1990).
15. Wernsdorfer, W. *et al.* Experimental evidence of the Neel–Brown model of magnetization reversal. *Phys. Rev. Lett.* **78**, 1791–1794 (1997).
16. Leighton, C. *et al.* Coercivity enhancement above the Neel temperature of an antiferromagnet/ferromagnet bilayer. *J. Appl. Phys.* **92**, 1483–1488 (2002).
17. Fitzsimmons, M. R. *et al.* Influence of in-plane crystalline quality of an antiferromagnet on perpendicular exchange coupling and exchange bias. *Phys. Rev. B.* **65**, 134436 (2002).
18. Braganca, P. M. *et al.* Reducing the critical current for short-pulse spin-transfer switching of nanomagnets. *Appl. Phys. Lett.* **87**, 112507 (2005).
19. Donahue, M. J. & Porter, D. G. *OOMMF User's Guide, Version 1.0 Interagency Report NISTIR 6376* (National Institute of Standard and Technology, Gaithersburg, MD, 1999).
20. Blundell, S. *Magnetism in Condensed Matter* 188–189 (Oxford Univ. Press, Oxford, 2001).
21. Gruyters, M. J. Structural and magnetic properties of transition metal oxide/metal bilayers prepared by *in situ* oxidation. *J. Magn. Magn. Mater.* **248**, 248–257 (2002).
22. Khapikov, A. F., Harrell, J. W., Fujiwara, H. & Hou, C. Temperature dependence of exchange field and coercivity in polycrystalline NiO/NiFe film with thin antiferromagnetic layer: Role of antiferromagnet grain size distribution. *J. Appl. Phys.* **87**, 4954–4956 (2000).
23. Sun, J. Z. Spin-current interaction with a monodomain magnetic body: A model study. *Phys. Rev. B* **62**, 570–578 (2000).
24. Compton, R. L., Pechan, M. J., Maat, S. & Fullerton, E. E. Probing the magnetic transitions in exchange-biased $FePt_3$/Fe bilayers. *Phys. Rev. B.* **66**, 054411 (2002).
25. Dubowik, D. *et al.* Temperature dependence of ferromagnetic resonance in permalloy/NiO exchange-biased films. *Eur. Phys. J. B* **45**, 283–288 (2005).
26. Slonczewski, J. C. Currents and torques in metallic magnetic multilayers. *J. Magn. Magn. Mater.* **247**, 324–338 (2002).
27. Nadgorny, B. *et al.* Transport spin-polarization of Ni_xFe_{1-x}: Electron kinematics and band structure. *Phys. Rev. B* **61**, R3788–R3791 (2000).
28. Fuchs, G. D. *et al.* Spin-torque ferromagnetic resonance measurements of damping in nanomagnets. *Appl. Phys. Lett.* **91**, 062507 (2007).

Supplementary Information accompanies this paper on www.nature.com/naturematerials.

Acknowledgements

We thank J. C. Sankey for providing us with the macrospin simulation code and T. Hauet for helpful discussions. This work was supported in part by the Semiconductor Research Corporation, the Office of Naval Research, the NSF/NSEC program through the Cornell Center for Nanoscale Systems and an IBM-Faculty Partnership award. The work was carried out in part at the Cornell NanoScale Facility, a member of the National Nanotechnology Infrastructure Network, which is supported by the National Science Foundation (Grant ECS 03-35765), and it benefited from use of the facilities of the Cornell Center for Materials Research, which is supported by the NSF/MRSEC program.

Author information

Reprints and permission information is available online at http://npg.nature.com/reprintsandpermissions. Correspondence and requests for materials should be addressed to O.O.